Nano-Micro Letters

e-ISSN 2150-5551
CN 31-2103/TB

ARTICLE

https://doi.org/10.1007/s40820-025-01846-6

Cite as
Nano-Micro Lett.
(2025) 17:328

Received: 10 April 2025
Accepted: 15 June 2025

Self-Regulated Bilateral Anchoring Enables Efficient Charge Transport Pathways for High-Performance Rigid and Flexible Perovskite Solar Cells

Haiying Zheng[1,4], Guozhen Liu[2] ✉, Xinhe Dong[4], Feifan Chen[4], Chao Wang[4],
Hongbo Yu[1], Zhihua Zhang[1] ✉, Xu Pan[3] ✉

HIGHLIGHTS

- Robust interface molecular bridge was constructed by employing self-transforming squaric acid (SA) to reduce residual stress and passivate defects at the buried interface.
- Attributing to the efficient charge transport pathways, the SA-modified perovskite solar cells demonstrate high photovoltaic performance with power conversion efficiency up to 25.50% (rigid) and 24.92% (flexible).
- The SA-modified devices demonstrate excellent stability under various environmental stress conditions, including humidity, thermal aging, light irradiation, and bending.

ABSTRACT Interface modification has been demonstrated as an effective means to enhance the performance of perovskite solar cells. However, the effect depends on the anchoring mode and strength of the interfacial molecules, which determines whether long-term robust interface for carrier viaduct can be achieved under operational light illumination. Herein, we select squaric acid (SA) as the interfacial molecule between the perovskite and SnO_2 layer and propose a self-regulated bilateral anchoring strategy. The unique four-membered ring conjugated structure and dicarboxylic acid groups facilitate stable hydrogen bonds and coordination bonds at both SnO_2/SA and SA/PbI_2 interfaces. The self-transforming property of SA enables the dynamic bilateral anchoring at the buried interface, ultimately releasing residual stress and constructing a stable interfacial molecular bridge. The results show that SA molecular bridge not only can effectively inhibit the generation of diverse charged defects but also serves as an effective electron transport pathway, resulting in improved power conversion efficiency (PCE) from 23.19 to 25.50% and excellent stability at the maximum power point. Additionally, the PCEs of the flexible and large-area (1 cm^2) devices were increased to 24.92% and 24.01%, respectively, demonstrating the universal applicability of the bilateral anchoring to PSCs based on different substrates and larger area.

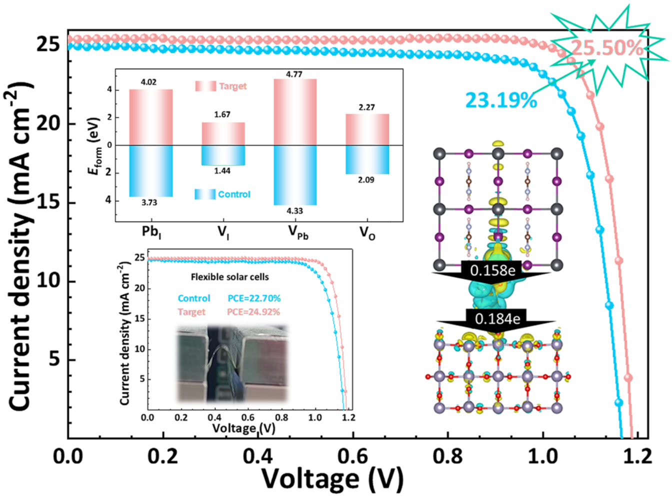

KEYWORDS Perovskite solar cells; Buried interface; Bilateral bonding; Defects passivation; Electron transport pathway

---

✉ Guozhen Liu, gzliu@dlut.edu.cn; Zhihua Zhang, zhzhang@djtu.edu.cn; Xu Pan, xpan@rntek.cas.cn
[1] School of Materials Science and Engineering, Dalian Jiaotong University, Dalian 116028, People's Republic of China
[2] State Key Laboratory of Fine Chemicals, School of Chemistry, Dalian University of Technology, Dalian 116024, People's Republic of China
[3] Key Laboratory of Photovoltaic and Energy Conservation Materials, Institute of Solid State Physics, Hefei Institutes of Physical Science, Chinese Academy of Sciences, Hefei 230031, People's Republic of China
[4] Institutes of Physical Science and Information Technology, Anhui University, Hefei 230601, People's Republic of China

1 Introduction

Perovskite solar cells (PSCs) have emerged as highly promising candidates for next-generation photovoltaic technology, characterized by their superior power conversion efficiency (PCE) and cost-effective manufacturing [1–5]. Within PSCs, the buried interface between the electron transport layer (ETL) and the perovskite absorber plays a pivotal role in charge extraction and overall device performance. SnO_2 has garnered significant attention as a widely employed ETL in PSCs, owing to its exceptional electron transport properties and commendable stability [6–8]. However, despite its advantages, the SnO_2 is inherently limited by challenges such as a high defect density, diminished charge extraction efficiency, and inadequate coordination [9–11]. These limitations can lead to detrimental outcomes, including charge recombination and a consequential reduction in open-circuit voltage (V_{oc}), thereby impairing device performance. Furthermore, the buried interface between the perovskite and SnO_2 substrate critically influences the crystallization kinetics of the perovskite film, which is a factor of paramount importance in optimizing device performance [12–14].

To address these challenges, substantial research efforts have been dedicated to modifying the SnO_2 buried interface in PSCs through various approaches, including additive engineering, surface modification techniques, and the incorporation of functional groups or nanoparticles [15–18]. For instance, Tian et al. introduced a cage polyamine molecule, 1,4-diazabicyclo[2,2,2]octane (DABCO), as a modulator at the SnO_2 buried interface to regulate the interface properties and enhance device performance [19]. Yang et al. developed DL-Carnitine hydrochloride (DL) as a multifunctional interfacial modifier, which effectively passivated buried defects and improved the quality of the perovskite film [20]. Guo et al. employed glycocyamine (GDA) as a molecular modifier to establish a molecular bridge at the SnO_2/perovskite buried interface, resulting in enhanced interfacial performance [21]. These studies collectively aim to achieve better energy level alignment, reduce defect density, and improve charge extraction and device stability. Zhou et al. revealed that the performance of perovskite at the buried interface differs significantly from that at the surface and PSCs are primarily illuminated from the bottom during operation, the buried interface exerts a much stronger influence on material properties than the surface [22]. However, due to its non-exposed nature, existing characterization techniques struggle to achieve nondestructive probing of the buried interface [23, 24]. Moreover, Ji et al. pointed out that materials commonly employed to modify the buried interface, such as NaI, NaCl, KI and choline iodide (ChI), are susceptible to dissolution or erosion in the dimethylformamide (DMF) and dimethyl sulfoxide (DMSO) solvents of the perovskite precursor solution, which significantly compromises their effectiveness in regulating the buried interface and further increases the challenges associated with studying this critical region [25, 26]. Therefore, the development of a multifunctional buried interface modification material that can remain stable in complex chemical environments and the elucidation of its modulation capabilities are essential for advancing the optoelectronic performance and stability of PSCs.

In this study, we developed a simple yet effective strategy to precisely regulate the SnO_2-based buried interface by introducing squaric acid (SA) as an interfacial molecular bridge. SA with self-transforming nature can form hydrogen bonds and coordination bonds with both the perovskite and SnO_2 at the buried interface under different chemical environments, thereby achieving multiple objectives: it passivates charged defects within the perovskite, fills oxygen vacancies (V_O) on the SnO_2 surface, and regulates perovskite crystal growth, ultimately yielding high-quality perovskite films with large grain sizes. In addition, SA adjusts the energy levels, serving as an efficient electron transport pathway that facilitates electron transfer from the perovskite to SnO_2 and reduces carrier recombination. The results demonstrate that SA-treated PSCs exhibit a significantly enhanced power conversion efficiency (PCE) of 25.50%, up from 23.19%, accompanied by improved environmental, thermal, and operational stability. Furthermore, large-area rigid (1 cm^2) and flexible PSCs based on the multifunctional buried interface achieve high PCEs of 24.01% and 24.92%, respectively. Notably, the bending stability of flexible PSCs is significantly improved due to the release of internal stress, highlighting the practical potential of this approach.

https://doi.org/10.1007/s40820-025-01846-6

2 Experimental Section

2.1 Materials

Lead iodide (PbI_2) was bought from TCI. Tin (IV) oxide (SnO_2) colloidal dispersion (15 wt% in H_2O) was purchased from Alfa Aesar. Formamidine iodide (FAI), methylamine hydrochloride (MACl), methylammonium bromide (MABr), Spiro-OMeTAD, Lithium bis (trifluoromethyl sulfonyl) imine (Li-TFSI) and 4-tert-butylpyridine (tBP) were acquired from Xi'an Polymer Light Technology Corp. Squaric acid (≥ 98%), isopropanol (IPA), lead bromide ($PbBr_2$), dimethyl sulfoxide (DMSO), chlorobenzene (CB), dimethylformamide (DMF) and acetonitrile (ACN) were purchased from Aladdin. ITO-PEN with a thickness of about 125 µm was purchased from Peccell Technologies, Inc. (Japan). All materials were used as purchased, without additional purification or modification.

2.2 Device Fabrication

ITO-coated glass substrates were ultrasonically cleaned sequentially in detergent, deionized water, and ethanol (20 min each), followed by oven drying. UV-ozone treatment (20 min) was performed prior to SnO_2 deposition. A SnO_2 colloidal dispersion (100 µL of 1 mg mL^{-1} NH_4Cl in deionized water) was spin-coated (4000 r min^{-1}, 30 s), and the films were annealed at 90 °C for 1 h. After that, SA solutions (0, 3, 5, 7 and 9 mg mL^{-1} in deionized water) were spin-coated (4000 r min^{-1}, 30 s) onto the SnO_2 layer, followed by annealing (100 °C, 10 min). After UV-ozone exposure (20 min), the substrates were transferred to a glovebox (RH: 20$–30%) for perovskite deposition. The precursor solution $(CsPbI_3)_{0.025}(FAPbI_3)_{0.825}(MAPbBr_3)_{0.15}$ (1.5 M Pb^{2+}, with 30% MACl) dissolved in a DMF:DMSO (4:1 v/v) mixture was stirred at 60 °C for 2 h. The precursor solution (50 µL) was spin-coated (1100 r min^{-1} for 10 s, 4500 r min^{-1} for 36 s) onto ITO/SnO_2/SA substrates, with chlorobenzene antisolvent added at the last 15 s. The films were annealed at 105 °C for 50 min. Afterward, the perovskite films were treated with 2-methylthio-2-imidazoline hydroiodide (4 mg mL^{-1} in IPA, 3000 r min^{-1}, 20 s) and annealed (100 °C, 10 min) to passivate defects and enhance V_{oc} [27]. After cooling to room temperature, Spiro-OMeTAD solution, consists of 73.5 mg spiro-OMeTAD, 29 µL tBP, 17 µL Li-TFSI (500 mg mL^{-1} in ACN) and 8 µL Co^{3+} salt (400 mg mL^{-1} in ACN) in 1 mL CB, was spin-coated (3000 r min^{-1}, 30 s). Finally, a 60-nm Au electrode was thermally evaporated (Quorum Q150TE Plus) through a mask (active area: 0.049 cm^2).

2.3 Characterizations

X-ray photoelectron spectroscopy (XPS) measurements were performed using an ESCALAB Xi + spectrometer (Thermo Fisher Scientific) equipped with an Al Kα X-ray. Ultraviolet photoelectron spectroscopy (UPS) analysis was conducted on an AXIS ULTRA DLD system (Shimadzu/Kratos) with a He I (21.22 eV) excitation source. In-situ GIWAXS data at the spin-coating stage were collected at beamline BL14B1 of the Shanghai Synchrotron Radiation Facility using an X-ray wavelength of 1.54 Å. Fourier transform infrared (FTIR) spectroscopy was carried out with a VERTEX 70v vacuum FTIR spectrometer, while UV–Vis absorption spectra were recorded on a Hitachi U-3900H spectrophotometer. X-ray diffraction (XRD) patterns were obtained by in situ charge and discharge X-ray diffractometer (D2 PHASER). Morphological characterization and cross-sectional analysis of perovskite films and devices were performed by field-emission scanning electron microscopy (FE-SEM, Gemini SEM300). Steady-state photoluminescence (PL) spectra were measured using Fluorescence spectrometer (FLS-1000). The time-resolved photoluminescence (TRPL) spectra were collected by FLS980 with a 485 nm pulsed laser. Grazing Incidence X-ray Diffraction (GIXRD) patterns were acquired by using a Rigaku Smartlab with Cu Kα radiation in the 2θ range of 30°-33°. Current density–voltage (*J-V*) curves were measured by a Keithley 2400 digital sourcemeter under AM 1.5G solar light (100 mW cm^{-2}), which was provided by an AAA class solar simulator (Newport Oriel Class 3A Model: 94043A). The external quantum efficiency (EQE) spectra were obtained by the quantum efficiency measurement system (QE-R, Enlitech, Taiwan of China). Electrochemical impedance spectroscopy (EIS) measurements (1 Hz-1 MHz) were performed using a Zennium CIMPS-pro setup (Germany). Contact angle measurements were conducted using an OCA15EC goniometer (Dataphysics, Germany). The device's performance was measured using the Candlelight System (Switzerland) under continuous white-LED illumination (1 sun), *J-V* curves were measured every 1 h.

Mechanical stability of the flexible devices was tested by a mechanical tester (PR-BDM-100, Puri, China).

2.4 Computational Details

First-principles calculations were conducted using density functional theory (DFT) within the Vienna Ab Initio Simulation Package (VASP) [28, 29]. The exchange–correlation interactions were described by the generalized gradient approximation (GGA) in the Perdew–Burke–Ernzerhof (PBE) formulation [29, 30]. A plane-wave energy cutoff of 480 eV was employed, with a convergence threshold of 10^{-4} eV for electronic relaxation. To mitigate spurious interlayer coupling, a 20 Å vacuum layer was introduced. Brillouin zone sampling was performed using a $2 \times 2 \times 1$ Monkhorst–Pack k-point grid. Structural optimization was continued until atomic forces fell below 0.05 eV $Å^{-1}$. Post-processing and structural visualization were facilitated by the VASPKIT and VESTA software packages [31, 32].

3 Results and Discussion

3.1 Chemical Interaction and Defect Passivation

Herein, we introduced a new molecule, SA, to modify the buried interface. SA is a symmetrical planar biprotic quaternary carbon oxygen compound with unique 2π-quasi-aromatic properties and reversible self-transformation structures (Fig. S1), which can act as both a hydrogen bond donor and acceptor and an effective electron transport pathway. By DFT simulation, we obtained the electrostatic potential (ESP) of SA in Fig. 1a. There is a relatively positive electron cloud density at the H atom (blue region) and a relatively negative electron cloud density at the O atom (red and yellow region), indicating that the O atom is able to interact strongly with Pb^{2+} [33], passivating the defect while becoming the active site of perovskite crystallization. Furthermore, we studied the interaction of perovskite and SA by XPS. The characteristic signal of Pb 4*f* in the target perovskite film moves toward the low binding energy position (Fig. 1b), reflecting the Lewis acid base coordination interaction between the O atom in the SA and the undercoordinated Pb^{2+} in the perovskite film. In addition, the XPS peaks of I 3*d* (Fig. 1c) and N 1 *s* (Fig. S2) show evident displacement, which are mainly caused by the strong hydrogen bond interaction between SA molecules and I^- and FA^+/MA^+ in perovskite.

Due to the special reversible self-transformation structures of SA, it can not only strongly interact with perovskite components to simultaneously passivate Pb-related defects, FA^+/MA^+ vacancy defects and I^-/Br^- vacancy defects in perovskite, but also can effectively fill the V_O on the surface of SnO_2 (Fig. S3). To verify the defect passivation effect of SA on SnO_2 and perovskite, by DFT method (The detailed DFT calculation methods are provided in in Supporting Information), we calculated the formation energy (E_{form}) of various defects at the interface between SnO_2 and perovskite before and after the introduction of SA (Figs. 1d-g and S4-S6, Table S1). At the FAI-terminated surface, there are mainly FA vacancy (V_{FA}), I vacancy (V_I) and V_O defects. As shown in Figs. 1d, e and S4, the E_{form} of V_{FA}, V_I and V_O in the reference system is calculated to be 3.97, 1.69, and 3.15 eV, respectively. In contrast, these values in target system increase to 4.12, 2.90, and 3.34 eV, respectively. At the PbI_2-terminated surface, the E_{form} of the main defects for I-site substitution by Pb antisite defect (Pb_I), Pb vacancy (V_{Pb}), I vacancy (V_I) and V_O are 4.02, 1.67, 4.77, and 2.27 eV (Figs. 1f, g and S5, S6), which is significantly higher than the defect E_{form} without SA [27, 34, 35]. The results show that SA has obvious passivation effect on various defects at the interface of SnO_2 and perovskite.

3.2 Interfacial Electron Transport and Photoelectric Performance of SnO_2

We compared XPS spectra to certify the effect of SA on the chemical environment of SnO_2 layer. As can be seen from Fig. 2a, the Sn 3*d* peaks of the SnO_2 film are, respectively, 495.28 and 486.78 eV, which shift to 495.68 and 487.28 eV for SA + SnO_2, meaning that the decreased electron density after SA modification and the existence of SA on the surface of SnO_2. In Fig. 2b, the O 1*s* signal of the control SnO_2 film can be decoupled into two peaks of 530.78 and 532.38 eV, which is attributed to the lattice oxygen (Sn–O-Sn) and V_O on the surface of SnO_2. In SA + SnO_2 film, the two peaks shift to 531.28 and 532.98 eV and the peak intensity of V_O decreases, indicating that the V_O is occupied by O atom or OH of SA and the surface non-radiative recombination could be inhibited [21, 26]. The movement of Sn 3*d* and O 1*s*

https://doi.org/10.1007/s40820-025-01846-6

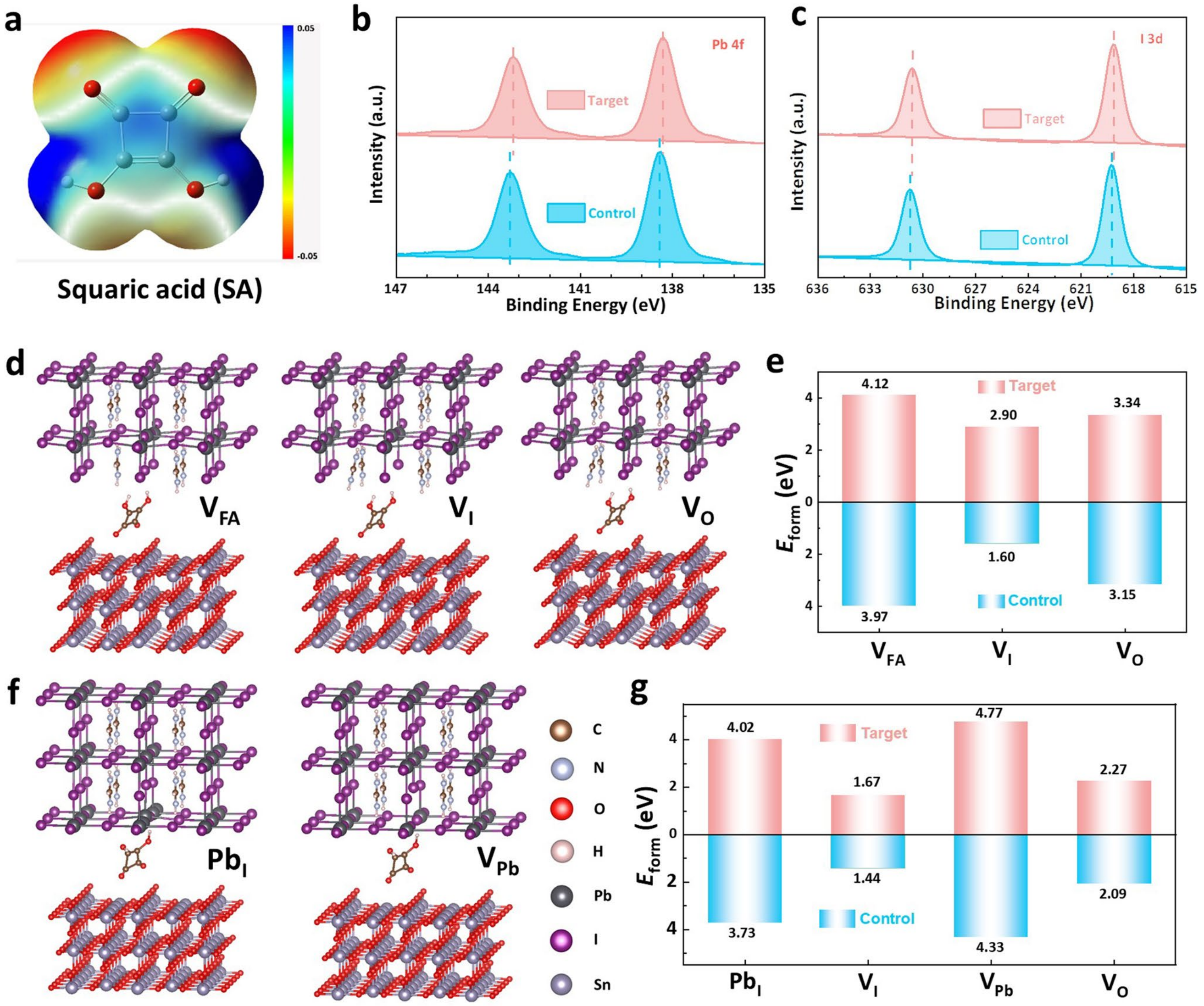

Fig. 1 Chemical interaction and defect formation energy. **a** ESP profiles of SA. XPS spectra of **b** Pb 4f and **c** I 3*d* of the control and target perovskite films. **d** Theoretical models of V_{FA}, V_I and V_O defect formation at the interface of SnO_2/SA/ perovskite with the FAI-terminated surface. **e** E_{form} of V_{FA}, V_I and V_O defect at the FAI-terminated surface for the control and target perovskite films. **f** Theoretical models of Pb_I and V_{Pb} defect formation at the interface of SnO_2/SA/perovskite with the PbI_2-terminated surface. **g** E_{form} of Pb_I, V_I, V_{Pb} and V_O defect at the PbI_2-terminated surface for the control and target perovskite films

peaks reveals a strong chemical interaction between SA and SnO_2 [26]. In addition, we also used FTIR spectroscopy to study the interaction between SA and SnO_2. In the FTIR spectra (Fig. S7), after SA modification, the Sn–O-Sn bond displays evident blue shift from 558 (for SnO_2) to 565 cm^{-1} (for $SnO_2 + SA$). In $SnO_2 + SA$ sample, the stretching vibration peaks of = C–O–C, C-O, -C = O and out-of-plane bending vibration peak of -OH move from 632, 1049, 1166, and 1812 cm^{-1} to 640, 1057, 1172, and 1819 cm^{-1}, respectively. These results all indicate the strong chemical interaction between SA and SnO_2.

In addition, the reversible self-transforming structure of SA makes it become as an electron transport channel between perovskite and SnO_2, allowing electrons to be transported rapidly through it (Fig. S1). To quantitatively assess charge transport at the SnO_2/perovskite interface, the 3D charge density difference and average Bard charge were calculated using DFT, as shown in Fig. 2c. The 3D charge density difference visually illustrates the detailed nature of

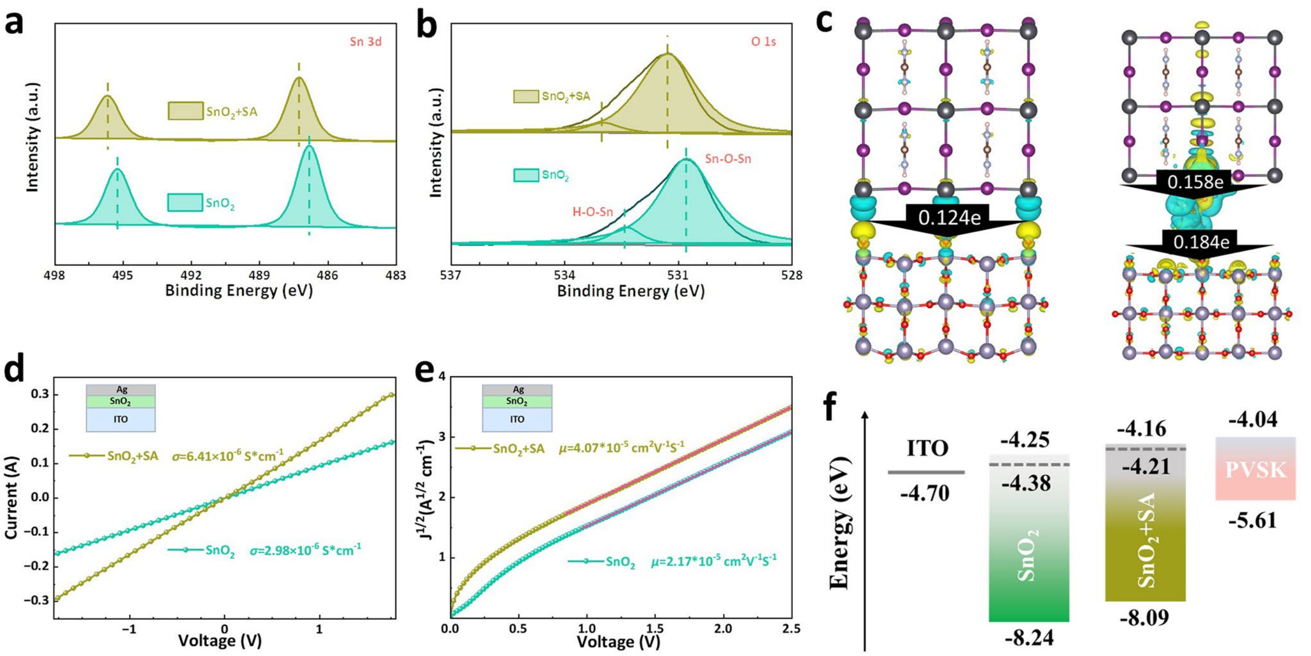

Fig. 2 Influence of SA on charge transport and photoelectric properties of SnO_2. XPS spectra of **a** Sn 3d and **b** O 1 *s* for the SnO_2 and SnO_2 + SA films. **c** 3D charge density difference and Bader charge analysis at the buried SnO_2/perovskite and SnO_2/SA/perovskite interface. **d** Conductivity measurement of SnO_2 and SnO_2 + SA films. **e** Electron transport properties of the SnO_2 and SnO_2 + SA determined by the SCLC. **f** Schematic diagram of the energy level arrangement before and after SA modification

charge transfer of the SA at the buried SnO_2/perovskite interface, where blue clouds represent electron losses relative to bonds or atoms after charge redistribution, and yellow clouds represent electrons captured relative to atoms [36–38]. It shows the prominent difference in charge density between the two interface structures, which is also reflected in the change in Bader charge. At the SnO_2/perovskite interface, a charge of 0.124e is transferred from the perovskite to the SnO_2 layer. In contrast, at the SnO_2/SA/perovskite interface, the calculated charges of 0.158e and 0.184e are transferred from perovskite to SA and SA to SnO_2, respectively [38, 39]. Both differential charge density and Bader charge analysis reveal that the introduction of SA leads to the remarkable difference in charge density at the SnO_2/perovskite interface and SA as a charge transport channel can effectively promote carrier transfer.

Then, we studied the effect of SA on the photoelectric performance of SnO_2. As can be seen from Fig. S8, the SA modification does not observably change the transmittance of SnO_2 layer. Then, in Fig. 2d, the conductivity of SnO_2 and SnO_2 + SA ETLs was calculated using the formula: $\sigma = Id/VA$, where A is effective area, d is thickness of ETLs [40, 41]. The conductivity of SnO_2 film with SA is slightly improved from 3.10×10^{-6} to 6.61×10^{-6} S cm^{-1}, due to the presence of SA charge transfer molecular bridges and the strong chemical interaction between SA and SnO_2. Next, in Fig. 2e, the electron mobility of SnO_2 was measured using space charge-limited current (SCLC), and the curves are fitted according to the Mott-Gurney equation: $J = 9\mu\varepsilon_0\varepsilon_r V^2/(8L^3)$ [41, 42]. The electron mobility of SnO_2 + SA and SnO_2 films are 5.88×10^{-3} and 3.22×10^{-3} cm^2 V^{-1} s^{-1}, respectively. The result further proves that SA modification enhances the electron transport of SnO_2, which is in agreement with the theoretical calculation results in Fig. 2c. The band structure of SnO_2 and SnO_2 + SA was characterized by UPS, as shown in Figs. S9, S10, and Table S2. The band conduction minimum (CBM) of SnO_2 and SnO_2-SA ETL was derived from the valence band maximum (VBM), and the band gap (E_g) values were determined by UV–vis absorption spectra and Tauc plots (Fig. S12). The CBM of SnO_2 + SA is closer to the CBM of perovskite than that of the original SnO_2 (Fig. 2f). A better alignment of energy levels between perovskite and SnO_2 + SA helps avoid carrier build-up at the interface and increases V_{oc} [26, 43, 44].

3.3 Crystallization and Morphology of Perovskite Films

The surface morphologies of SnO_2 before and after SA modification were firstly studied by top-view scanning electronic microscope (SEM) images. The original SnO_2 nanoparticles are densely packed onto the ITO substrate (Fig. 3a). The deposition of SA obscures the GBs of these SnO_2 nanoparticles, meaning that thin and continuous SA layer is successfully deposited on SnO_2 layer (Fig. 3b). Furthermore, to investigate the role of SA in the crystallization of perovskite films, the time-dependent in-situ GIWAXS patterns was performed at the spin-coating stage. As shown in Fig. 3c, d, at the instant of antisolvent drops (approximately 18 s), the perovskite film on the SA-modified SnO_2 layer exhibits a stronger δ-phase FA perovskite signal (Qz $\approx$8.34 nm^{-1}) than the control film. In the subsequent process, compared with the control sample, the target perovskite film dispalys quickly appeared α phase FA perovskite signal (Qz $\approx$9.91 nm^{-1}) at about 45 s along with the continuedly increased intensity, meanwhile, the δ phase FA peak gradually decreases [45, 46]. The results indicatie that δ phase FA perovskite is transformed into α phase FA perovskite more quickly, which means that SA is beneficial to lead a more effective and faster phase transition process to reduce the hidden danger caused by the difficulty of converting mesophase crystals into photoactive phases [47, 48].

From Figs. 3e, f and S13, it can be clearly seen that the perovskite grown on the SA-modified SnO_2 layer has a better morphology with more uniform, reduced GBs and larger grain sizes (Fig. S14). The improved crystallinity of the target perovskite film induced by SA stems from strong interactions between SA and perovskite, which can reduce the number of nucleation centers and lead to the formation of a uniform crystalline structure with larger grain sizes. In addition, the root mean square (RMS) roughness of the perovskite films before and after modification was investigated by atomic force microscopy (AFM) measurements (Fig. 3g, h). The RMS of the control and target films is 33.43 and 29.07 nm, respectively. The reduced roughness also

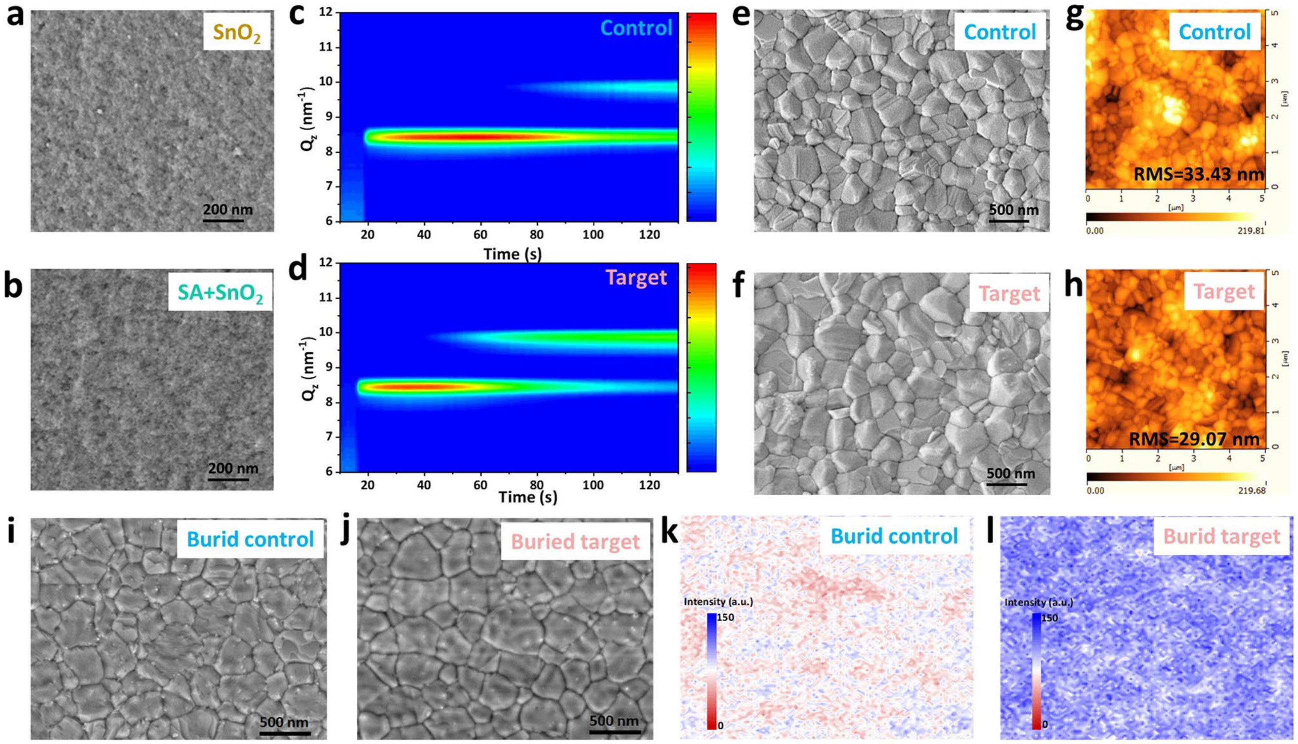

Fig. 3 Influence of SA on crystallization and morphology of perovskite films. Top-view SEM images of **a** SnO_2 and **b** SnO_2+SA films. 2D contour map obtained from the time-dependent in-situ GIWAXS patterns of the **c** control and **d** target perovskite films at the spin-coating stage. **e, f** Top-view SEM images and **g, h** AFM images of the control and target perovskite films. **i, j** Top-view SEM images and **k, l** PL mapping images of the buried interface from the bottom of the control and target perovskite films peeled off from SnO_2 and SnO_2+SA

indicates that SA is conducive to uniform nucleation and crystallization of perovskite film.

Subsequently, to further evaluate the influence of the buried interface with and without SA on the growth of perovskite, the morphology and PL properties of the buried interface were studied by SEM images and PL mapping tests. The results (Fig. 3i, j) are consistent with those measured by top-view SEM images (Fig. 3e, f). The perovskite film grown on $SnO_2 + SA$ displays denser structure with larger grain size and smaller grain boundaries. In contrast, the SnO_2-based perovskite film has more irregular crystals. As shown in Fig. 3k, l, in comparison with the buried control film, the buried target perovskite film displays observably enhanced overall fluorescence localization intensity with more uniform distribution, indicating that the significantly suppressed non-radiative recombination caused by surface defects. These results indicate that the SA-treated SnO_2 layer can promote the growth of perovskite crystals, finally to obtain high quality and low defect target film.

3.4 Carrier Dynamics and Residual Stress Investigation

The quality of perovskite layer with perovskite/SnO_2/glass structure was further studied by using XRD patterns and UV–vis absorption spectra. As can be seen in Figs. S16 and S17, and Table S3, the SA-modified perovskite film displays higher diffraction peak intensities and smaller full width at half maximum (FWHM) values for the (110) lattice planes, meaning that the SA-modified SnO_2 is conducive to the growth of perovskite crystals, resulting in increased crystallinity and improved film quality. In Fig. S18, the slightly increased absorption intensity in the UV–vis absorption spectra predicts that the quality of the target perovskite film is higher. Furthermore, the charge transport behavior of the perovskite films on the SnO_2 without and with SA studied by using steady-state PL spectra and time-resolved TRPL spectra. According to PL spectra in Fig. 4a, the PL intensity of the perovskite layer after SA modification is significantly reduced, indicating that SA not only passivates the interface to promote perovskite crystallization but also facilitates the electron transport between SnO_2 and perovskite, endowing it with higher film quality, lower defect density and reduced non-radiation recombination. TRPL spectra in Fig. 4b were recorded to quantitatively compare the charge transfer of the control and target perovskite films. The average PL decay lifetime of the target perovskite film reduces from 228.76 ns for control film to 139.24 ns. The shorter average PL decay lifetime indicates a much faster charge transfer process from perovskite to SnO_2, which is mainly caused by the greatly reduced defect density in target perovskite film and is likely to contribute to better photovoltaic performance.

We collected the charge transfer resistance (R_{ct}) and carrier recombination resistance (R_{rec}) in the device by EIS under dark conditions with an applied voltage of −1.0 V in Fig. 4c. Compared with the control device, the R_{ct} of the target device is significantly reduced from 892.46 to 516.01 Ω and the R_{rec} is significantly increased from 1511.54 to 2323.42 Ω, indicating that the target device has a faster charge transfer rate and a slower carrier recombination rate. The trap density of perovskite device is calculated by space charge current limiting (SCLC) technique. The electron-only devices with the structure of ITO/SnO_2/perovskite/PCBM/Au were prepared. The corresponding dark *J-V* curves are exhibited in Fig. 4d, and the trap-filling voltage (V_{TFL}) can be obtained. V_{TFL} of the devices before and after treatment are 0.57 and 0.28 V, respectively. The trap density (N_t) was calculated from $N_t = 2V_{TFL}\varepsilon_0\varepsilon_r/(qL^2)$. The N_t of the control and target perovskite devices were 4.75×10^{15} and 1.97×10^{15} cm^{-3}, respectively. The results show that the defects of target perovskite are effectively suppressed owing to its higher film quality.

Dark *J-V* curves (Fig. 4e) were measured to further investigate the charge transfer and recombination behavior of PSCs. The reverse leakage current density and dark saturation current density (J_0) of the target perovskite device are smaller, indicating that the reduced bulk defect, improved charge extraction, effectively inhibited charge recombination and increased V_{oc} [49]. The result is consistent with the EIS results of a decrease in R_{tr} and an increase in R_{rec}. The dependence of light intensity on J_{sc} and V_{oc} has also been used to investigate the effect of SA on charge extraction and defect passivation of target perovskites. As shown in Fig. S19, the α value of the target perovskite device (0.997) is closer to 1 than that of the control device (0.918), implying the fast separation of the photogenerated electron–hole pairs and inhibited trap-assisted carrier recombination in the target perovskite device, due to the better energy level matching between $SA + SnO_2$ and perovskite. Figure 4f shows the logarithmic relationship of V_{oc} with light intensity, where the slope of the line is n kB/T. When n value is greater than and close to 1, which means the appearance of defect assisted

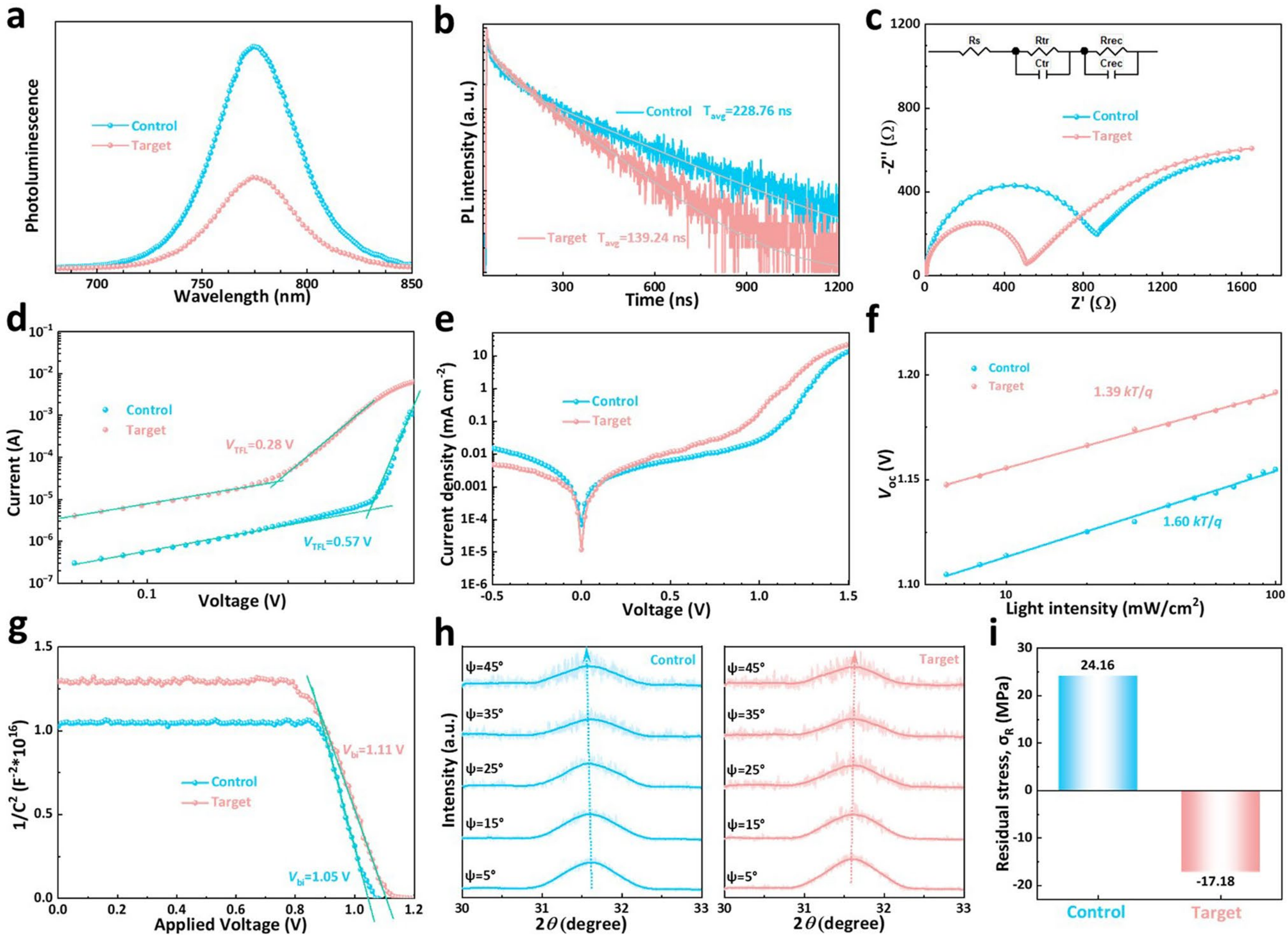

Fig. 4 Carrier Dynamics and Residual Stress of perovskite films and devices. **a** Steady-state PL spectra and **b** TRPL spectra of the control and target perovskite/SnO_2/ITO without and with SA. **c** Nyquist plots at V = -1.0 V, **d** Dark current–voltage (I-V) curves with the configurations of electron-only (glass/ITO/SnO_2/perovskite/passivation layer/PCBM/Au), **e** Dark J-V curves, **f** V_{oc} values of the corresponding devices versus light intensity on a seminatural logarithmic scale and **g** Mott-Schottky plots of the control and target perovskite devices. **h** GIXRD patterns measured at different ψ angles from 5° to 45° and **i** comparison of residual stress for the control and target perovskite films

recombination and reduction of defect assisted recombination in the PSCs, respectively. It can be seen from Fig. 4f that the n value of the target perovskite device is significantly reduced, which proves that the target perovskite device displays fewer defects, thus reducing the non-radiative recombination and increasing the V_{oc}. Mott-Schottky plots were used to evaluate the improvement of V_{oc} and built-in potential (V_{bi}) in perovskite devices. In Fig. 4g, the V_{bi} values of the control and target perovskite devices are 1.05 and 1.11 V, respectively. The target device exhibits higher V_{bi}, indicating that the built-in band alignment on heterogeneous structures, which makes the more efficient carrier collection at the perovskite/ETL interface [50].

The SA has beneficial impacts on the morphology and crystallinity of perovskite, which also influence the release of residual stress. Therefore, we investigated the residual stress of the perovskite films using GIXRD (Fig. 4h). The results show that the diffraction peaks of the control perovskite gradually shift to lower 2θ positions as ψ changes from 5 to 45°, whereas the diffraction peaks of the target perovskite slightly move to higher 2θ positions. According to Bragg's Law and generalized Hooke's Law, the relationship between 2θ and $\sin^2\psi$ can be expressed by the following equation: $\sigma = -E_p \pi \cot\theta_0/[2(1+\nu_p)180°]*\partial(2\theta)/\partial[(\sin^2\psi)]$ (E_p is the perovskite modulus (10 GPa), ν_p is Poisson's ratio of the perovskite (0.3) and θ_0 is half of the scattering angle $2\theta_0$ for stress-free perovskite ($2\theta_0$ = 31.6°)) [51]. By fitting 2θ as a function of $\sin^2\psi$ (Fig. S20), the residual stress in the perovskite films can be calculated using the above equation. The slope of the fitted line indicates the magnitude of residual strain. Negative slope means that the film endures tensile stress, whereas positive slope represents the film undergoes compressive stress [51–53]. The calculated results are shown in Fig. 4i, revealing that the control perovskite subjects a tensile stress of 24.6 MPa. In contrast, the target perovskite film exhibits a slight compressive stress (−17.18 MPa). It indicates that the introduction of SA can release the residual tensile stress in the perovskite film, which is beneficial for improving the PCE and stability of PSCs [53].

3.5 Photovoltaic Performance and Stability

Based on the structure of ITO/SnO_2/perovskite/passivation layer/spiro-OMeTAD/Au (Fig. 5a), we investigated the effect of the introduction of SA on photovoltaic performance of PSCs. The optimized *J-V* curve under reverse and forward scan directions with a scan speed of 0.05 V s^{-1} of the champion devices (When the concentration of SA is 5 mg mL^{-1}) and the corresponding photovoltaic parameters are shown in Fig. 5b and Table S6. The champion PCE of target devices improves significantly from 23.19% of control devices to 25.50%, mainly due to the increase in V_{oc} (from 1.17 to 1.19 V), J_{sc} improvement (from 25.04 to 25.47 mA cm^{-2}) and FF improvement (from 79.46 to 84.30%). After calculation, the target device also exhibits a lower hysteretic index than the control device, declining from 3.10% (for control) to 0.94%, which may be caused by the simultaneous reduced the bulk and interface to effectively prevent ion diffusion [54].

Figure 5c displays the EQE spectra of the corresponding PSCs, demonstrating the superior performance of the target PSC in enhancing J_{sc}. Furthermore, to investigate the delay and reproducibility of the PSCs, we monitored both the stabilized power output (SPO) at maximum V_{oc} (V_m) over 1000 s under continuous one-sun illumination (Fig. 5d). To further verify the effective role of SA, we also fabricated large-area perovskite devices and flexible PSCs and the corresponding *J-V* curves are shown in Fig. 5e, f. The large-area rigid PSC (1 cm^2) based on SA yields a PCE of 24.01% and exhibits significantly reduced hysteresis (Fig. 5e). The target flexible PSC (0.049 cm^2) delivers a considerable PCE of 24.92%, which is much higher than that of control device (22.70%). Moreover, the hysteresis index analysis reveals a decrease from 3.44% (control) to 1.57% for the target flexible device. Figure 5g shows the statistical photovoltaic parameters for the control and target rigid and flexible PSCs and the target rigid and flexible PSCs demonstrate better reproducibility and higher average photovoltaic parameters. The results show that SA contributes to an overall enhancement in V_{oc}, J_{sc} and FF of both rigid and flexible devices, and thus improving PCE. These outstanding photovoltaic properties highlight the potential of SA as a multifunctional interlayer that can be widely used to manufacture highly efficient PSCs.

Subsequently, we verified the long-term stability of perovskite devices at 45 ± 5% RH and 85 °C, respectively (Figs. S23-S29). Firstly, we observed the actual morphological changes of target perovskite film, all perovskite films were placed in a moisture-aged environment (Fig. S23). The control film gradually changes from black to brown to pale yellow, showing serious degradation. In contrast, there is few noticeable differences in the target film, indicating its excellent moisture resistance due to reduced bulk and surface defect. Then, we performed water contact angle measurements to verify the high hydrophobic property of target perovskite film (Fig. S24). It can be seen that the contact angle of the target perovskite film (90.6°) is much larger than that of the control film (75.1°), indicating its better hydrophobicity. Figure S25 also shows the humidity stability of unsealed PSCs under 45 ± 5% RH at room temperature. After 3840 h of aging, the PCE of the control PSC decreases to 64% of the original value, while the target PSC still retains more than 93% of the initial PCE. Figure S27 examines the thermal stability of unencapsulated PSCs under 20% RH at 85 °C. The target device maintains about 88% of their initial PCE after 528 h, in contrast, the PCE of control device drops to 57% of the original value. We also compared the light absorption intensity of the perovskite films during thermal aging. As shown in Fig. S29, with the progress of temperature aging, the absorption intensity of the control film decreases rapidly, while the decline rate of the target film is significantly lower, which can maintain about 93% of its initial absorption intensity after 500 h of aging at 85 °C, suggesting that it has better thermal resistance.

In addition, more rigorous stability measurements were conducted on both control and target perovskite devices. The operational stability of unencapsulated devices was evaluated under continuous 1-sun illumination at maximum power point tracking (MPPT) in a nitrogen (N_2) atmosphere at room

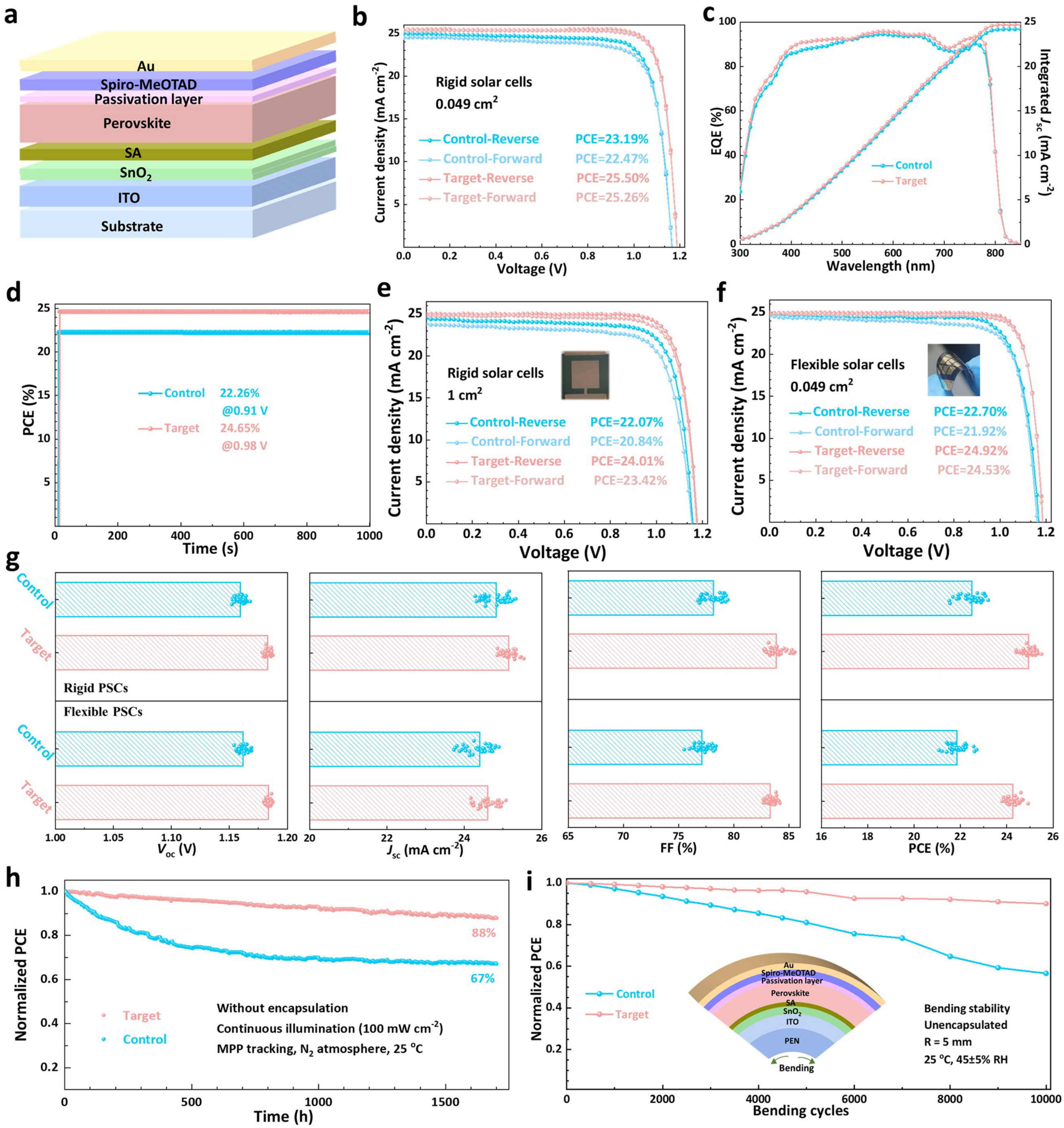

Fig. 5 Photovoltaic performance and stability of PSCs. **a** Schematic architecture of the fabricated PSCs. **b** *J-V* curves under reverse and forward scan directions, **c** EQE spectra and **d** stabilized PCE at maximum power point as a function of time of the control and target perovskite devices. **e** *J-V* curves of the large-area rigid PSCs (1 cm^2) and **f** *J-V* curves of flexible PSCs under reverse and forward scan directions. **g** Statistics of the photovoltaic parameters for the control and target rigid and flexible PSCs. **h** Normalized PCE of the unencapsulated control and target PSCs measured at MPP under continuous 1-sun illumination in ambient atmosphere and at room temperature. **i** Normalized PCE variation curves of the unencapsulated control and target flexible PSCs over the bending cycle at R = 5 mm

temperature. The corresponding changes in PCE are shown in Fig. 5h. It can be observed that the control device exhibits significant PCE degradation, retaining only 67% of its initial PCE after 1700 h. In contrast, the target device demonstrates markedly enhanced operational stability, and maintains 88% of its original PCE after the same period. Figure 5i presents the results of bending stability tests for the control and target PSCs under ambient conditions. With a bending radius (R) of 5 mm, the PCE of the control device rapidly decreases as the number of bending cycles increases, dropping to 56% of its initial PCE after 10,000 cycles. Whereas, the target perovskite device presents enhanced mechanical stability, maintaining over 90% of its original PCE after the same number of bending cycles. The overall stability enhancement of the target perovskite device primarily stems from the role of SA in improving perovskite film quality, reducing defects, suppressing ion migration, strengthening interfacial connections, and dynamically releasing residual stress under external environmental stress. This further validates the advantages of the self-management bilateral bonding effect of SA.

4 Conclusions

In summary, SA, due to its unique structure, exhibits self-managed bilateral bonding characteristics, enabling comprehensive modulation of the buried interface between SnO_2 and the perovskite layer, which significantly enhances the PCE and stability of PSCs. Firstly, SA interacts with SnO_2, Pb^{2+}, FA^+/MA^+, and I^-/Br^-, effectively filling surface oxygen vacancies and passivating defects in the perovskite layer, thereby improving the interface quality. Secondly, while adjusting the energy levels of SnO_2, SA serves as a charge transport channel through structural self-transformation, which facilitat the transfer of electrons from the perovskite to the SnO_2 ETL, thereby improving interfacial charge transfer and reducing carrier recombination. Finally, SA acts as a nucleation center to regulate the crystal growth of the perovskite, resulting in high-quality perovskite films with increased grain size and preferential orientation. Consequently, the SA-modified PSCs demonstrate significant improvements in J_{sc}, V_{oc}, and FF, achieving a high PCE of 25.50%. Notably, large-area rigid (1 cm^2) and flexible devices yield excellent PCEs of 24.01% and 24.92%, respectively. Additionally, the unencapsulated SA-modified devices display excellent stability under environmental stress, including humidity, thermal aging, light irradiation, and bending conditions. This study provides valuable insights into the rational design of multifunctional molecules with self-transformation properties for optimizing the buried interface of perovskite materials, paving the way for their practical application and commercialization in highly efficient and stable PSCs.

Acknowledgements This work was financially supported by the National Natural Science Foundation of China (Grant 52102196 and 52402228), China Postdoctoral Science Foundation (Grant 2023M740474) and Postdoctoral Fellowship Program of CPSF (GZB20230095).

Author Contributions GL, XP and ZZ have proposed the concept and directed the research. HZ, GL and HD performed the preparation of materials and devices. FC and CW carried out the characterization of materials and devices. HZ and GL finished writing the manuscript. HY, XP and ZZ put forward suggestions on the research. All the authors participated in the discussion of the results.

Declarations

Conflict of interest The authors declare no interest conflict. They have no known competing financial interests or personal relationships that could have appeared to influence the work reported in this paper.

Supplementary Information The online version contains supplementary material available at https://doi.org/10.1007/s40820-025-01846-6.

References

1. H. Chen, X. Pan, W. Liu, M. Cai, D. Kou et al., Efficient panchromatic inorganic–organic heterojunction solar cells with consecutive charge transport tunnels in hole transport material.

Chem. Commun. **49**(66), 7277–7279 (2013). https://doi.org/10.1039/C3CC42297F

2. M. Ma, C. Zhang, Y. Ma, W. Li, Y. Wang et al., Efficient and stable perovskite solar cells and modules enabled by tailoring additive distribution according to the film growth dynamics. Nano-Micro Lett. **17**(1), 39 (2024). https://doi.org/10.1007/s40820-024-01538-7
3. Z. Shao, Z. Wang, Z. Li, Y. Fan, H. Meng et al., A scalable methylamine gas healing strategy for high-efficiency inorganic perovskite solar cells. Angew. Chem. Int. Ed. **58**(17), 5587–5591 (2019). https://doi.org/10.1002/anie.201814024
4. C. Zhao, H. Zhang, A. Krishna, J. Xu, J. Yao, Interface engineering for highly efficient and stable perovskite solar cells. Adv. Opt. Mater. **12**(7), 2301949 (2024). https://doi.org/10.1002/adom.202301949
5. National Renewable Energy Laboratory (NREL), Best research-cell efficiencies chart. http://www.nrel.gov/pv/assets/images/efficiency-chart.png (Accessed: January 2025).
6. Y. Zhao, F. Ma, Z. Qu, S. Yu, T. Shen et al., Inactive $(PbI_2)_2RbCl$ stabilizes perovskite films for efficient solar cells. Science **377**(6605), 531–534 (2022). https://doi.org/10.1126/science.abp8873
7. Y. Ren, K. Zhang, Z. Lin, X. Wei, M. Xu et al., Long-chain gemini surfactant-assisted blade coating enables large-area carbon-based perovskite solar modules with record performance. Nano-Micro Lett. **15**(1), 182 (2023). https://doi.org/10.1007/s40820-023-01155-w
8. Z. Shen, Q. Han, X. Luo, Y. Shen, T. Wang et al., Crystal-array-assisted growth of a perovskite absorption layer for efficient and stable solar cells. Energy Environ. Sci. **15**(3), 1078–1085 (2022). https://doi.org/10.1039/D1EE02897A
9. A. Uddin, H. Yi, Progress and challenges of SnO_2 electron transport layer for perovskite solar cells: a critical review. Sol. RRL **6**(6), 2100983 (2022). https://doi.org/10.1002/solr.202100983
10. K. Wei, J. Deng, L. Yang, C. Zhang, M. Huang et al., A Core@Dual–shell nanostructured SnO_2 to modulate the buried interfaces toward stable perovskite solar cells with minimized energy losses. Adv. Energy Mater. **13**(4), 2203448 (2023). https://doi.org/10.1002/aenm.202203448
11. X. Liu, J. Min, Q. Chen, T. Liu, G. Qu et al., Synergy effect of a π-conjugated ionic compound: dual interfacial energy level regulation and passivation to promote voc and stability of planar perovskite solar cells. Angew. Chem. Int. Ed. **61**(11), e202117303 (2022). https://doi.org/10.1002/anie.202117303
12. L. Chen, Z. Liu, L. Qiu, J. Xiong, L. Song et al., Multifunctional regulation of SnO_2 nanocrystals by snail mucus for preparation of rigid or flexible perovskite solar cells in air. ACS Nano **17**(23), 23794–23804 (2023). https://doi.org/10.1021/acsnano.3c07784
13. C. Deng, J. Wu, Y. Yang, Y. Du, R. Li et al., Modulating residual lead iodide *via* functionalized buried interface for efficient and stable perovskite solar cells. ACS Energy Lett. **8**(1), 666–676 (2023). https://doi.org/10.1021/acsenergylett.2c02378
14. Y. Xu, X. Guo, Z. Lin, Q. Wang, J. Su et al., Perovskite films regulation *via* hydrogen-bonded polymer network for efficient and stable perovskite solar cells. Angew. Chem. Int. Ed. **62**(33), e202306229 (2023). https://doi.org/10.1002/anie.202306229
15. X. Yang, D. Luo, Y. Xiang, L. Zhao, M. Anaya et al., Buried interfaces in halide perovskite photovoltaics. Adv. Mater. **33**(7), 2006435 (2021). https://doi.org/10.1002/adma.202006435
16. Z.-W. Gao, Y. Wang, W.C.H. Choy, Buried interface modification in perovskite solar cells: a materials perspective. Adv. Energy Mater. **12**(20), 2104030 (2022). https://doi.org/10.1002/aenm.202104030
17. Q. Fu, X. Tang, Y. Gao, H. Liu, M. Chen et al., Dimensional tuning of perylene diimide-based polymers for perovskite solar cells with over 24% efficiency. Small **19**(24), 2301175 (2023). https://doi.org/10.1002/smll.202301175
18. F. Li, X. Deng, Z. Shi, S. Wu, Z. Zeng et al., Hydrogen-bond-bridged intermediate for perovskite solar cells with enhanced efficiency and stability. Nat. Photonics **17**(6), 478–484 (2023). https://doi.org/10.1038/s41566-023-01180-6
19. J. Tian, J. Wu, R. Li, Y. Lin, J. Geng et al., Cage polyamine molecule modulating the buried interface of tin oxide/perovskite in photovoltaic devices. Nano Energy **118**, 108939 (2023). https://doi.org/10.1016/j.nanoen.2023.108939
20. L. Yang, H. Zhou, Y. Duan, M. Wu, K. He et al., 25.24%-efficiency FACsPbI3 perovskite solar cells enabled by intermolecular esterification reaction of DL-carnitine hydrochloride. Adv. Mater. **35**(16), 2211545 (2023). https://doi.org/10.1002/adma.202211545
21. H. Guo, W. Xiang, Y. Fang, J. Li, Y. Lin, Molecular bridge on buried interface for efficient and stable perovskite solar cells. Angew. Chem. Int. Ed. **62**(34), e202304568 (2023). https://doi.org/10.1002/anie.202304568
22. Y. Zhou, L.M. Herz, A.K. Jen, M. Saliba, Advances and challenges in understanding the microscopic structure–property–performance relationship in perovskite solar cells. Nat. Energy **7**(9), 794–807 (2022). https://doi.org/10.1038/s41560-022-01096-5
23. S. Xiong, S. Jiang, Y. Zhang, Z. Lv, R. Bai et al., Revealing buried heterointerface energetics towards highly efficient perovskite solar cells. Nano Energy **109**, 108281 (2023). https://doi.org/10.1016/j.nanoen.2023.108281
24. B. Chen, H. Chen, Y. Hou, J. Xu, S. Teale et al., Passivation of the buried interface *via* preferential crystallization of 2D perovskite on metal oxide transport layers. Adv. Mater. **33**(41), 2103394 (2021). https://doi.org/10.1002/adma.202103394
25. C. Gong, C. Zhang, Q. Zhuang, H. Li, H. Yang et al., Stabilizing buried interface *via* synergistic effect of fluorine and sulfonyl functional groups toward efficient and stable perovskite solar cells. Nano-Micro Lett. **15**(1), 17 (2022). https://doi.org/10.1007/s40820-022-00992-5
26. X. Ji, L. Bi, Q. Fu, B. Li, J. Wang et al., Target therapy for buried interface enables stable perovskite solar cells with 2505% efficiency. Adv. Mater. **35**(39), 2303665 (2023). https://doi.org/10.1002/adma.202303665

27. G. Liu, H. Zheng, J. Ye, S. Xu, L. Zhang et al., Mixed-phase low-dimensional perovskite-assisted interfacial lead directional management for stable perovskite solar cells with efficiency over 24%. ACS Energy Lett. **6**(12), 4395–4404 (2021). https://doi.org/10.1021/acsenergylett.1c01878
28. G. Kresse, J. Hafner, *Ab initio*molecular dynamics for open-shell transition metals. Phys. Rev. B **48**(17), 13115–13118 (1993). https://doi.org/10.1103/physrevb.48.13115
29. J.P. Perdew, K. Burke, M. Ernzerhof, Generalized gradient approximation made simple. Phys. Rev. Lett. **77**(18), 3865–3868 (1996). https://doi.org/10.1103/physrevlett.77.3865
30. W. Kohn, L.J. Sham, Self-consistent equations including exchange and correlation effects. Phys. Rev. **140**(4A), A1133–A1138 (1965). https://doi.org/10.1103/physrev.140.a1133
31. V. Wang, N. Xu, J.-C. Liu, G. Tang, W.-T. Geng, VASPKIT: a user-friendly interface facilitating high-throughput computing and analysis using VASP code. Comput. Phys. Commun. **267**, 108033 (2021). https://doi.org/10.1016/j.cpc.2021.108033
32. K. Momma, F. Izumi, *VESTA*: a three-dimensional visualization system for electronic and structural analysis. J. Appl. Crystallogr. **41**(3), 653–658 (2008). https://doi.org/10.1107/s0021889808012016
33. Y. Yang, T. Zhao, M.-H. Li, X. Wu, M. Han et al., Passivation of positively charged cationic defects in perovskite with nitrogen-donor crown ether enabling efficient perovskite solar cells. Chem. Eng. J. **451**, 138962 (2023). https://doi.org/10.1016/j.cej.2022.138962
34. Y. Zhang, R. Yu, M. Li, Z. He, Y. Dong et al., Amphoteric ion bridged buried interface for efficient and stable inverted perovskite solar cells. Adv. Mater. **36**(1), 2310203 (2024). https://doi.org/10.1002/adma.202310203
35. Y. Liu, Q. Liu, Y. Lu, J. Fu, J. Wu et al., Polyfluorinated organic diammonium induced lead iodide arrangement for efficient two-step-processed perovskite solar cells. Angew. Chem. Int. Ed. **63**(26), e202402568 (2024). https://doi.org/10.1002/anie.202402568
36. W. Shao, H. Wang, S. Fu, Y. Ge, H. Guan et al., Tailoring perovskite surface potential and chelation advances efficient solar cells. Adv. Mater. **36**(24), e2310080 (2024). https://doi.org/10.1002/adma.202310080
37. C. Shi, Q. Song, H. Wang, S. Ma, C. Wang et al., Molecular hinges stabilize formamidinium-based perovskite solar cells with compressive strain. Adv. Funct. Mater. **32**(28), 2201193 (2022). https://doi.org/10.1002/adfm.202201193
38. H. Xu, Z. Liang, J. Ye, Y. Zhang, Z. Wang et al., Constructing robust heterointerfaces for carrier viaduct *via* interfacial molecular bridges enables efficient and stable inverted perovskite solar cells. Energy Environ. Sci. **16**(12), 5792–5804 (2023). https://doi.org/10.1039/D3EE02591H
39. G. Qu, Y. Qiao, J. Zeng, S. Cai, Q. Chen et al., Enhancing perovskite solar cell performance through dynamic hydrogen-mediated polarization of nitrogen and sulfur in phthalocyanine. Nano Energy **118**, 108974 (2023). https://doi.org/10.1016/j.nanoen.2023.108974
40. Z. Li, C. Wang, P.-P. Sun, Z. Zhang, Q. Zhou et al., *In-situ* peptization of WO_3 in alkaline SnO_2 colloid for stable perovskite solar cells with record fill-factor approaching the Shockley–queisser limit. Nano Energy **100**, 107468 (2022). https://doi.org/10.1016/j.nanoen.2022.107468
41. Z. Li, Z. Wan, C. Jia, M. Zhang, M. Zhang et al., Cross-linked polyelectrolyte reinforced SnO_2 electron transport layer for robust flexible perovskite solar cells. J. Energy Chem. **85**, 335–342 (2023). https://doi.org/10.1016/j.jechem.2023.06.026
42. H. Ma, M. Wang, Y. Wang, Q. Dong, J. Liu et al., Asymmetric organic diammonium salt buried in SnO_2 layer enables fast carrier transfer and interfacial defects passivation for efficient perovskite solar cells. Chem. Eng. J. **442**, 136291 (2022). https://doi.org/10.1016/j.cej.2022.136291
43. X. Ji, K. Feng, S. Ma, J. Wang, Q. Liao et al., Interfacial passivation engineering for highly efficient perovskite solar cells with a fill factor over 83. ACS Nano **16**(8), 11902–11911 (2022). https://doi.org/10.1021/acsnano.2c01547
44. Z. Qin, Y. Chen, X. Wang, N. Wei, X. Liu et al., Zwitterion-functionalized SnO_2 substrate induced sequential deposition of black-phase $FAPbI_3$ with rearranged PbI_2 residue. Adv. Mater. **34**(32), 2203143 (2022). https://doi.org/10.1002/adma.202203143
45. S. Li, Y. Jiang, J. Xu, D. Wang, Z. Ding et al., High-efficiency and thermally stable $FACsPbI_3$ perovskite photovoltaics. Nature **635**(8037), 82–88 (2024). https://doi.org/10.1038/s41586-024-08103-7
46. X. Li, Y. Li, Y. Feng, J. Qi, J. Shen et al., Strain regulation of mixed-halide perovskites enables high-performance wide-bandgap photovoltaics. Adv. Mater. **36**(23), e2401103 (2024). https://doi.org/10.1002/adma.202401103
47. T. Niu, L. Chao, Y. Xia, K. Wang, X. Ran et al., Phase-pure α-$FAPbI_3$ perovskite solar cells *via* activating lead-iodine frameworks. Adv. Mater. **36**(13), e2309171 (2024). https://doi.org/10.1002/adma.202309171
48. Z. He, S. Zhang, Y. Gao, Q. Geng, X. Jia et al., Multi-site anchoring of single-molecule for efficient and stable perovskite solar cells with lead shielding. J. Energy Chem. **87**, 390–399 (2023). https://doi.org/10.1016/j.jechem.2023.08.041
49. J. Song, Q. Hu, Q. Zhang, S. Xiong, Z. Zhao et al., Manipulating the crystallization kinetics by additive engineering toward high-efficient photovoltaic performance. Adv. Funct. Mater. **31**(14), 2009103 (2021). https://doi.org/10.1002/adfm.202009103
50. Z. Song, Y. Gao, Y. Zou, H. Zhang, R. Wang et al., Single-crystal-assisted *in situ* phase reconstruction enables efficient and stable 2D/3D perovskite solar cells. J. Am. Chem. Soc. **146**(2), 1657–1666 (2024). https://doi.org/10.1021/jacs.3c12446
51. C. Shao, J. Ma, G. Niu, Z. Nie, Y. Zhao et al., Strain release *via* glass transition temperature regulation for efficient and stable perovskite solar cells. Adv. Mater. **37**(10), e2417150 (2025). https://doi.org/10.1002/adma.202417150
52. X. Chang, J.-X. Zhong, S. Li, Q. Yao, Y. Fang et al., Two-second-annealed 2D/3D perovskite films with graded energy funnels and toughened heterointerfaces for efficient and durable

solar cells. Angew. Chem. Int. Ed. **62**(38), e202309292 (2023). https://doi.org/10.1002/anie.202309292

53. S. Liu, J. Li, W. Xiao, R. Chen, Z. Sun et al., Buried interface molecular hybrid for inverted perovskite solar cells. Nature **632**(8025), 536–542 (2024). https://doi.org/10.1038/s41586-024-07723-3

54. G. Richardson, S.E.J. O'Kane, R.G. Niemann, T.A. Peltola, J.M. Foster et al., Can slow-moving ions explain hysteresis in the current–voltage curves of perovskite solar cells? Energy Environ. Sci. **9**(4), 1476–1485 (2016). https://doi.org/10.1039/C5EE02740C